Journal of Materials Science & Technology 79 (2021) 205–211

Contents lists available at ScienceDirect

Journal of Materials Science & Technology

journal homepage: www.jmst.org

Research Article

A balance between catalysis and nanoconfinement towards enhanced hydrogen storage performance of $NaAlH_4$

Wei Chen [a], Lei You [c], Guanglin Xia [a,*], Xuebin Yu [a,b,**]

[a] Department of Materials Science, Fudan University, Shanghai, 200433, China
[b] Guangdong Provincial Key Laboratory of Advanced Energy Storage Materials, South China University of Technology, Guangzhou, 510640, China
[c] College of Chemistry and Chemical Engineering, Hubei University, Wuhan 430062, China

ARTICLE INFO

Article history:
Received 3 September 2020
Received in revised form 19 October 2020
Accepted 19 November 2020
Available online 24 December 2020

Keywords:
Sodium alanate
Hydrogen storage
Synergistic effect
Catalysis
Nanoconfinement

ABSTRACT

Owing to its favorable thermodynamics and high density, $NaAlH_4$ has been widely regarded as a potential hydrogen storage material, but its practical application is hindered by the sluggish kinetics, high operating temperature and poor cycling stability. Here, taking advantage of Co-doped nanoporous carbon scaffolds as structural host, we develop a new strategy to balance the synergistic effect between the catalytic role of Co nanoparticles and the nanoconfinement role of porous carbon scaffolds *via* the controllable etching of Co nanoparticles towards enhanced hydrogen storage performance of $NaAlH_4$. The etching of Co nanoparticles creates extra void spaces nearby catalytically active Co nanoparticles, which not only exerts the catalytic effect of Co nanoparticles, but also improves the nanoconfinement role in maintaining the cycling stability towards increased loading ratio and hence high systematic capacity. Induced by this balanced synergistic effect, the peak temperature for the dehydrogenation of $NaAlH_4$ could be reduced to 164 °C, 97 °C lower than the bulk counterpart, even under an ultrahigh loading ratio of 67 %, and more importantly, the reversible systematic hydrogen storage capacity could still reach 3.3 wt.% after 5 cycles. This work opens up a new avenue to improve the hydrogen storage performance of various complex hydrides.

1. Introduction

The use of reliable and renewable energy carriers obtains critical importance due to the increasing ecological issues caused by the massive consumption of fossil fuels. Hydrogen has attracted worldwide interest as an ideal energy carrier in the future due to its high energy density, reproducibility, and environmental friendliness with zero CO_2-emission [1–4]. The implementation of "hydrogen economy", however, is hindered due to the lack of efficient techniques for the safe storage of hydrogen with high energy density [5,6]. In this regard, complex hydrides, including borohydrides, amides, and alanates, are one of the most promising solid-state hydrogen storage systems because of their high gravimetric and volumetric hydrogen densities [7–11]. Among them, sodium alanate ($NaAlH_4$), possessing a high gravimetric (7.5 wt.%) and volumetric (94 g L^{-1}) hydrogen densities, is the only known complex hydride that holds relatively favorable thermodynamics that allows it to operate near the working temperatures of proton exchange membrane fuel cells [12]. Nevertheless, the high kinetic barriers due to the sluggish mass transport and the poor cycling stability still hinder its practical applications as on-board hydrogen storage materials [13].

In recent years, considerable efforts have been devoted to lowering the operating temperature and enhancing the reversibility of $NaAlH_4$ *via* introducing transition metal-based catalysts [14–26]. Among these catalysts, Co-based species have been theoretically and experimentally verified to be one of the most effective catalysts towards improving the hydrogen storage performance of $NaAlH_4$ [19–22]. The onset dehydrogenation temperature of $NaAlH_4$ could be reduced by around 100 °C with the addition of Co-decorated activated carbon as the catalysts [23]. The inevitable growth and agglomeration of catalysts and $NaAlH_4$ upon heating, however, leads to poor cycling stability. The other approach is to downsize the particle size into nanometer range by nanoconfining $NaAlH_4$ into porous substrates *via* melt and/or solution infiltration, which could directly reduce the diffusion pathway and hence relieve the

* Corresponding author.
** Corresponding author at: Department of Materials Science, Fudan University, Shanghai, 200433, China.
E-mail addresses: xiaguanglin@fudan.edu.cn (G. Xia), yuxuebin@fudan.edu.cn (X. Yu).

https://doi.org/10.1016/j.jmst.2020.11.052
1005-0302/

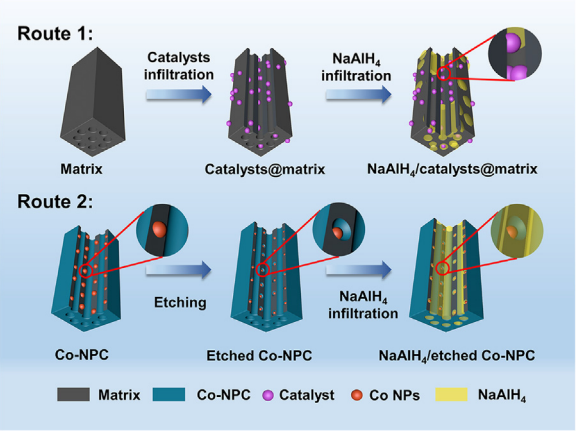

Fig. 1. Schematic illustration of the traditional method to fabricate nanoconfined $NaAlH_4$ with the addition of catalysts (Route 1) and the strategy adopted in this work to balance the synergistic effect of catalysis and nanoconfinement *via* the etching of Co NPs *in-situ* formed inside Co-NPC (Route 2).

inherent limitations to the diffusion of hydrogen in the solid state [27–32]. In addition, the porous scaffolds could physically alleviate the growth and agglomeration of $NaAlH_4$ NPs inside during cycling dehydrogenation and hydrogenation process upon thermal heating, leading to an improved cycling stability. Bearing these in mind, a synergistic combination between catalysts and nanoconfinement as illustrated by route 1 in Fig. 1 has been adopted to further improve the hydrogen storage performance of $NaAlH_4$, which could be achieved by step-by-step infiltration of catalysts and $NaAlH_4$ into porous scaffolds [33–37]. Nevertheless, the preliminary infiltration of catalysts could block pores of scaffolds, resulting in the inhomogeneous distribution of $NaAlH_4$ and the isolation of $NaAlH_4$ from the effective catalysts, which deteriorates the catalytic role of catalysts and the space-confinement role of nanoconfinement. Moreover, the infiltration of catalysts occupies the void space of porous scaffolds, which leads to further decrease of loading capacity of $NaAlH_4$ and hence the systematic hydrogen storage capacity. As a result, the practical hydrogen storage capacity of nanoconfined $NaAlH_4$ with the addition of catalysts reported in the previous literatures is usually lower than 50 % [27,34–37]. Therefore, the development of a facile strategy to nanoconfine $NaAlH_4$ with high capacity and homogeneous distribution with effective catalysts is highly desirable and, indeed, imperative for the practical applications as hydrogen storage materials.

Herein, in order to balance the synergistic effect of catalysis and nanoconfinement in improving the hydrogen storage performance of $NaAlH_4$ while maintaining a high storage capacity, Co NPs doped nanoporous carbon scaffolds (Co-NPC) derived from ZIF67 was adopted as scaffolds to realize an ultrahigh loading ratio of 67 % *via* the controllable etching of Co NPs. As illustrated by route 2 in Fig. 1, the etching partial Co NPs *in-situ* formed inside porous Co-NPC could not only provide more void space for the efficient infiltration of $NaAlH_4$ nearby catalytic Co NPs to achieve a high loading ratio and hence a high systematic hydrogen storage capacity, but also enhance the intimate contact between $NaAlH_4$ and Co NPs and thus promote the catalytic effect of Co towards superior hydrogen storage performance. Moreover, the porous structure of Co-NPC could effectively prevent the phase separation between $NaAlH_4$ and Co NPs and the growth and agglomeration of $NaAlH_4$ NPs, leading to a stable cycling performance. As a result, the nanoconfined $NaAlH_4$ NPs inside Co-NPC exhibit high systematic H_2 storage capacities with low dehydrogenation temperature, fast kinetics, and long-term cycling stability.

2. Results and discussion

Scanning electron microscopy (SEM) images (Fig. 2a) exhibited that the as-prepared ZIF-67 possessed a uniform dodecahedral structure with an average particle size of ~300 nm. X-ray diffraction (XRD) patterns (Fig. S1) confirmed the presence of the characteristic diffraction peaks of ZIF-67, indicating the successful synthesis of ZIF67. After carbonization under Ar atmosphere, the diffraction peaks of ZIF-67 completely disappeared with the appearance of new peaks that could be indexed to Co crystals, which demonstrates the complete carbonization of ZIF-67 to form Co NPs doped nanoporous carbon scaffolds (Co-NPC). As evidenced by SEM image (Fig. 2b), the thus-formed Co-NPC retained the original shapes of ZIF-67 and exhibited rough surfaces with a slight shrinkage in the skeletal structure to ~250 nm owing to the thermal effect. Transmission electron microscopy (TEM) results revealed that each Co-NPC showed a highly porous structure and Co NPs, as verified by high-resolution TEM (HRTEM) image (Fig. 2c), were well distributed inside the carbon matrix with an average particle size of 18.3 nm (Fig. S2). Subsequently, the porous structure of the as-prepared Co-NPC was quantitatively determined *via* N_2 adsorption-desorption isotherms (Fig. S3), which gave a Brunauer–Emmett–Teller (BET) surface area of 346.97 $m^2\ g^{-1}$ and a pore volume of 0.29 $cm^3\ g^{-1}$ with an average pore size of 2.47 nm. The porous structure of Co-NPC provides void spaces for the melt infiltration of $NaAlH_4$ while the presence of Co NPs could play a catalytic role in further enhancing the hydrogen storage performance of thus-formed $NaAlH_4$ NPs.

Subsequently, a melt-infiltration method was adopted to realize the nanoconfinement of $NaAlH_4$ into Co-NPC. After the infiltration of $NaAlH_4$ into Co-NPC, the diffraction peaks of both Co and $NaAlH_4$ could be clearly observed in the XRD results (Fig. S1, Supporting Information). Due to the porous structure of Co-NPC, no visible agglomeration of particles could be observed upon the increase of weight ratio from 25 % to 50 % (Fig. 2d), indicating the effective confinement of $NaAlH_4$. By comparison, upon increasing the weight ratio of $NaAlH_4$ over 60 %, there are some clear particles of $NaAlH_4$ aggregated on the surface of Co-NPC (Fig.s 2e, f), which could deteriorate the confinement and catalytic role of Co-NPC in improving the hydrogen storage performance of $NaAlH_4$.

In order to verify that, the hydrogen desorption performance of nanoconfined $NaAlH_4$ with various loading ratios were measured using temperature-dependent desorption (TPD) coupled with the relative differential curves (Fig. 3). In the differential curves (Fig. 3b), the onset and peak temperature of hydrogen release for ball-milled $NaAlH_4$ was as high as 185 °C and 261 °C. With the addition of Co NPs, the onset temperature for the dehydrogenation of $NaAlH_4$/Co could be reduced to 98 °C with two peak temperature observed at 183 °C and 224 °C, respectively, resulting from the dehydrogenation of $NaAlH_4$ to form Na_3AlH_6 and Al followed by the hydrogen desorption from Na_3AlH_6 to generate NaH and Al, which agrees well with the previously reported results [12,15]. This result directly demonstrates the catalytic role of Co in enhancing the hydrogen storage performance of $NaAlH_4$. In strong contrast, as expected, the onset and peak temperature of dehydrogenation could be significantly reduced after nanoconfinement into Co-NPC. Based on the pore volume of Co-NPC (*i.e.*, 0.29 $cm^3\ g^{-1}$), the maximum theoretical loading ratio of $NaAlH_4$ into Co-NPC is calculated to be 26 %. Hence, in the term of 25 % $NaAlH_4$/Co-NPC, the onset and peak temperature was decreased to 69 °C and 147 °C, which is 28 °C and 36 °C lower than that of Co-catalyzed $NaAlH_4$, respectively, indicating the important role of nanoconfinement in improving the hydrogen storage performance of $NaAlH_4$ due to the significant reduction of particle size to nanometer scale. In addition, only one major peak, corresponding to a single-step decomposition of $NaAlH_4$ into NaH and Al, could be observed during the

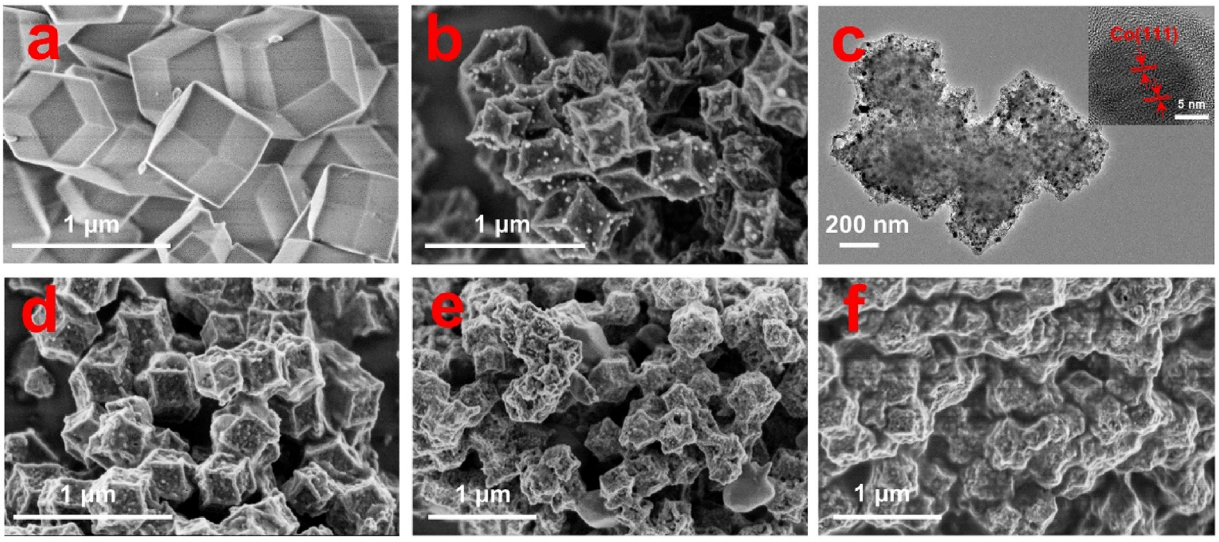

Fig. 2. SEM images of ZIF-67 (a) and Co-NPC (b). TEM images of Co-NPC (c) and the inset in (c) is the HRTEM image of Co-NPC. SEM images of 50 % $NaAlH_4$/Co-NPC (d), 60 % $NaAlH_4$/Co-NPC (e), and 67 % $NaAlH_4$/Co-NPC (f).

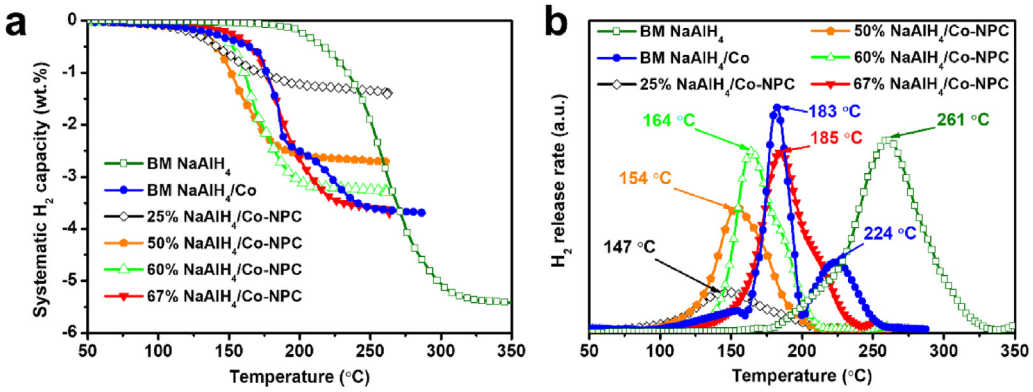

Fig. 3. TPD curves (a) and their differential curves (b) of $NaAlH_4$/Co-NPC with various loading ratios of $NaAlH_4$.

dehydrogenation of 25 % $NaAlH_4$/Co-NPC, which is different from bulk $NaAlH_4$ and the composite of $NaAlH_4$/Co. This phenomenon could be attributed to the significantly improved dehydrogenation kinetics of Na_3AlH_6 induced by the nanoconfinement role and the catalytic role of Co-NPC, which leads to the simultaneous proceeding of two-step dehydrogenation of $NaAlH_4$, thus manifesting a major peak [32]. Upon the increase of loading ratio to over 50 %, which leads to the agglomeration and particle growth of $NaAlH_4$ on the surface of Co-NPC due to the lack of enough void space for nanoconfining $NaAlH_4$ as shown in Figs. 2e and f, both the onset and peak temperature, however, increased. Specifically, the peak temperature for the dehydrogenation of $NaAlH_4$ with a loading ratio of 67 % was increased to 185 °C, which is already comparable to the ball-milled $NaAlH_4$ catalyzed by Co NPs. It corresponds well with the observation that serious agglomeration and growth of $NaAlH_4$ appeared on the surface of Co-NPC when increasing the loading ratio of $NaAlH_4$ to 67 % (Fig. 2f).

Although the nanoconfinement of $NaAlH_4$ into Co-NPC with a lower loading ratio below 50 % leads to superior hydrogen release performance of $NaAlH_4$ due to the effective confinement role and the catalytic effect of Co NPs, the decrease of loading ratios results in the tremendous reduction of systematic hydrogen storage capacity, *e.g.*, 1.4 wt.% for 25 % $NaAlH_4$/Co-NPC and 2.8 wt.% for 50 % $NaAlH_4$/Co-NPC (Fig. 3a). In order to solve this dilemma, the synergistic effect of catalysis and nanoconfinement was balanced *via* the controllable etching partial Co NPs to create more space for the infiltration of $NaAlH_4$ and meanwhile, decrease the content of catalysts. More importantly, the freshly created space nearby Co NPs could ensure the intimate contact between $NaAlH_4$ and Co NPs and hence improve the catalytic effect of Co NPs.

Thermogravimetric analysis (TGA) results (Fig. S4) verified that the original weight percentage of Co NPs in the as-prepared Co-NPC was around 41 %. Upon increasing the concentration of HNO_3 and etching time, the weight percentage of Co in the composite could be reduced to be 22 %, 12 %, and 4%, denoted as 22 % Co-NPC, 12 % Co-NPC, and 4% Co-NPC, respectively. After the etching process, XRD patterns (Fig. S4) of 22 % Co-NPC and 12 % Co-NPC still exhibited the diffraction peaks of Co crystals, while there is no diffraction peak for 4% Co-NPC, which could be mainly attributed to the low weight content of Co in the scaffold. SEM images (Fig. 4a-c) demonstrated that the morphology of Co-NPC after etching and reduction under H_2/Ar atmosphere could be well maintained. Typically, it is interesting to notice that the average particle size of Co NPs in 22 % Co-NPC was decreased to 12.9 nm, 5.4 nm smaller than the original Co NPs in Co-NPC (Fig. S2), which directly demonstrates that the etching of Co NPs could decrease the particle size of Co NPs and hence provide more space nearby Co NPs. To further verify the effect of the etching of Co NPs in improving the nanoconfinement of $NaAlH_4$, N_2 adsorption-desorption isotherms of 22 % Co-NPC (Fig. S3) was tested. It validates that the etching of Co NPs leads to the

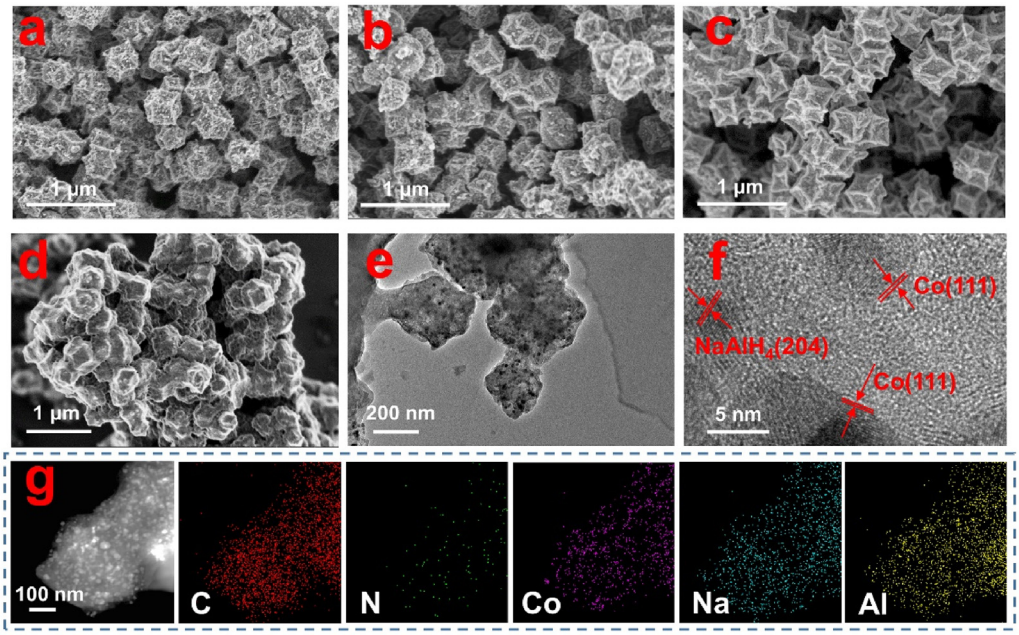

Fig. 4. SEM images of 22 % Co-NPC (a), 12 % Co-NPC (b), 4% Co-NPC (c), and 67 % $NaAlH_4$/22 % Co-NPC (d). TEM (e), HRTEM (f) and EDS elemental mapping (g) images of 67 % $NaAlH_4$/22 % Co-NPC.

increase of the BET surface area and the total pore volume to 402.16 $m^2\ g^{-1}$ and 0.38 $cm^3\ g^{-1}$ for 22 % Co-NPC, which is 15.9 % and 31.0 % higher than that of Co-NPC, respectively. Moreover, the average pore size of 22 % Co-NPC was increased from 2.47 nm to 2.82 nm after the etching process, which offers efficient pathways for the effective infiltration of $NaAlH_4$. The increase of both surface area and the pore volume provides more void space for nanoconfining $NaAlH_4$, which could not only improve the hydrogen storage performance of $NaAlH_4$, but also increase the loading ratio of $NaAlH_4$ towards high H_2 storage capacity.

In order to verify the effect of the etching of Co NPs on the hydrogen release performance of nanoconfined $NaAlH_4$, an ultrahigh loading ratio of 67 % infiltrated into various Co-NPC was selected. SEM image (Fig. 4d) revealed that, due to the creation of void spaces *via* the etching of Co NPs, the agglomeration of $NaAlH_4$ could be largely alleviated upon increasing the loading ratio to as high as 67 %. Typically, with a high loading ratio of 67 %, the rough framework of nanoporous carbon scaffolds could still be observed in 22 % Co-NPC (Fig. 4d), while serious agglomeration of Co-NPC was observed in 67 % $NaAlH_4$/Co-NPC (Fig. 2f), indicating the effective nanoconfinement of $NaAlH_4$ due to the increase of void space after etching of Co NPs. Moreover, the uniform distribution of $NaAlH_4$ and Co inside 67 % $NaAlH_4$/22 % Co-NPC could be further verified by TEM images (Fig. 4e) and the corresponding EDS elemental mapping results (Fig. 4g), which illustrated that the elemental mapping of Na and Al from $NaAlH_4$ and Co corresponded well with that of C and N from Co-NPC. HRTEM image (Fig. 4f) clearly showed the lattice planes of Co and $NaAlH_4$, indicating the presence of Co NPs and confined $NaAlH_4$ NPs. These results provide additional evidence to the fact that, due to the creation of extra spaces by the etching of Co NPs, $NaAlH_4$ was successfully and uniformly infiltrated into the etched Co-NPC during the melting infiltration process. As a result, the peak temperature for the dehydrogenation of nanoconfined $NaAlH_4$ was further decreased to a large content upon the etching of Co NPs (Fig. 5a). Among them, the hydrogen storage performance of 67 % $NaAlH_4$/22 % Co-NPC is the best, exhibiting a peak temperature of only 164 °C, which is 21 °C lower than the peak temperature of 67 % $NaAlH_4$/Co-NPC and is even comparable to that of 50 % $NaAlH_4$/Co-NPC. Although the maximum theoretical loading ratio of $NaAlH_4$ into 22 % Co-NPC is only 32 % according to the pore volume of 22 % Co-NPC (*i.e.*, 0.38 $cm^3\ g^{-1}$), the dehydrogenation of 67 % $NaAlH_4$/22 % Co-NPC is still capable of releasing 3.7 wt.% H_2 before 220 °C due to the synergistic effect of the catalytic role and the nanoconfinement role of 22 % Co-NPC. The systematic hydrogen storage capacity of 67 % $NaAlH_4$/22 % Co-NPC is 32 % higher than that of 50 % $NaAlH_4$/Co-NPC. By comparison, although more pore volume could be created by the excessive etching of Co NPs to a weight ratio of ~12 % and 4%, the peak temperature of 67 % $NaAlH_4$/12 % Co-NPC and 67 % $NaAlH_4$/4% Co-NPC, however, was increased to 176 °C and 183 °C, respectively, which could be attributed to the deteriorated catalytic effect due to the lack of enough catalysts. These results directly demonstrate the important role of the balance between catalysis and nanoconfinement in enhancing the hydrogen storage performance of $NaAlH_4$ with high systematic H_2 storage capacity. Considering both the operating temperature and the systematic hydrogen storage capacity, 67 % $NaAlH_4$/22 % Co-NPC was selected for detailed investigation as hydrogen storage materials.

Subsequently, the isothermal dehydrogenation kinetics of 67 % $NaAlH_4$/22 % Co-NPC were investigated at various temperatures (Fig. 5c). In the period of 30 min, a capacity of ~3.3 wt.% hydrogen could be released from 67 % $NaAlH_4$/22 % Co-NPC at 180 °C, which is 0.7 wt.% higher than 50 % $NaAlH_4$/Co-NPC. By comparison, under the identical condition, only a hydrogen capacity of 2.6 wt.% could be released from the ball-milled $NaAlH_4$ under the catalysis of Co NPs even at a temperature as high as 200 °C. It provides further evidence to the superior dehydrogenation performance of 67 % $NaAlH_4$/22 % Co-NPC due to the synergistic effect of catalysis from Co NPs and nanoconfinement. In addition, 67 % $NaAlH_4$/22 % Co-NPC could release ~3.0 wt.% hydrogen in 90 min upon lowering the operating temperature to 160 °C. To qualitatively understand the effect of etched Co-NPC in enhancing the hydrogen storage performance of 67 % $NaAlH_4$/22 % Co-NPC, the apparent activation energy (E_a) for the dehydrogenation from $NaAlH_4$ was calculated according to the isothermal dehydrogenation curves at various temperatures. As shown in Fig. 5d, by plotting ln(H_2 release rate) *versus* $1/T$ [38], E_a for the dehydrogenation of 67 % $NaAlH_4$/22 % Co-NPC was calculated to be 82.64 kJ mol^{-1}, which was ~45 kJ mol^{-1} lower than

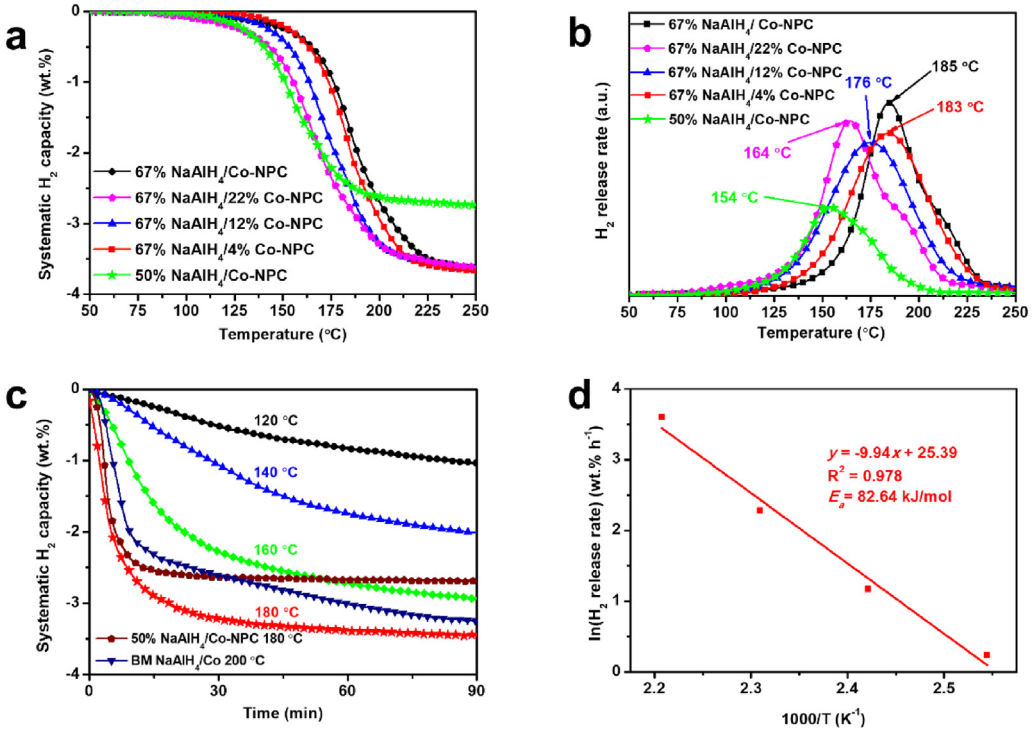

Fig. 5. TPD curves (a) and the relative differential curves (b) of $NaAlH_4$ nanoconfined into *x*% Co-NPC. (c) The isothermal dehydrogenation kinetics and (d) Arrhenius profiles of the dehydrogenation kinetics of 67 % $NaAlH_4$/22 % Co-NPC.

ball-milled $NaAlH_4$ [32,39]. The significant decrease of E_a provides additional support to the significant enhancement of the dehydrogenation kinetics for the 67 % $NaAlH_4$/22 % Co-NPC owing to the balanced synergistic effect of catalysis and nanoconfinement.

Owing to the sintering effect and phase separation of NaH and Al, the cycling performance of $NaAlH_4$ is another major obstacle for its practical application. Therefore, the hydrogen storage reversibility of 67 % $NaAlH_4$/22 % Co-NPC, in comparison with bulk $NaAlH_4$ catalyzed with Co NPs, was further investigated. As shown in Fig. 6a, under the catalysis of Co NPs, the H_2 capacity released from $NaAlH_4$ was tremendously reduced from 3.2 wt.% to 0.9 wt.% after only 2 cycles of reversible storage process even at a temperature as high as 200 °C. In strong contrast, the hydrogen released from 67 % $NaAlH_4$/22 % Co-NPC after 5 cycles of reversible hydrogenation and dehydrogenation process could still reach 3.3 wt.% at only 170 °C, corresponding to a capacity retention of 98 %, which directly demonstrates the favorable reversible storage performance of nanoconfined $NaAlH_4$ owing to the structural support role of 22 % Co-NPC. XRD patterns (Fig. 6b) demonstrated the formation of NaH and Al after 5 cycles of dehydrogenation, and the characteristic diffraction peaks of $NaAlH_4$ could be clearly recovered after subsequent rehydrogenation process, which provides additional evidence for the excellent reversibility of 67 % $NaAlH_4$/22 % Co-NPC. After cycling hydrogen storage process, SEM (Fig. 6c) and TEM (Fig. 6d) images of the 67 % $NaAlH_4$/22 % Co-NPC validated that the morphology of as-prepared 67 % $NaAlH_4$/22 % Co-NPC was well preserved without obvious change. In addition, by analyzing the HRTEM image of 67 % $NaAlH_4$/22 % Co-NPC after the fifth cycle of dehydrogenation process (Fig. 6e), the inter planar spacings of the nanoparticles inside 22 % Co-NPC were measured to be 0.202 nm and 0.205 nm, corresponding to (200) plane of Al and (111) plane of Co, respectively, which is in agreement with the XRD patterns (Fig. 6b). These results confirm the well distribution of $NaAlH_4$ inside 22 % Co-NPC after the cycling process. Moreover, the homogenous distribution of the dehydrogenated $NaAlH_4$ inside 22 % Co-NPC matrix could be further verified by the scanning TEM (STEM) image and the corresponding EDS elemental mapping results, which validated that the elemental mapping of Na and Al of the dehydrogenated $NaAlH_4$ and C and Co of 22 % Co-NPC matched well with the structure of 22 % Co-NPC, leading to the significantly enhanced cycling stability of $NaAlH_4$. The operating temperature, the cycling stability, and the reversible capacity of 67 % $NaAlH_4$/22 % Co-NPC, compared with previously reported works, are among the best of $NaAlH_4$ adopting nanoconfinement to improve its hydrogen storage performance (Table S1).

3. Conclusion

In summary, we have developed a facile strategy to balance the synergistic effect of catalysis and nanoconfinement in improving the hydrogen storage performance of $NaAlH_4$ with high systematic hydrogen storage density. By virtue of Co-doped nanoporous carbon as scaffolds, the etching of Co NPs inside Co-NPC leads to the creation of void space nearby active Co NPs with catalytic effects, which not only leads to an enhanced catalytic effect in promoting the hydrogen storage performance of $NaAlH_4$ but also improves the nanoconfinement role of Co-NPC in maintaining the cycling stability of $NaAlH_4$ with the increased loading ratio and thus enhanced systematic storage capacity. Particularly, with a loading ratio as high as 67 %, the dehydrogenation of $NaAlH_4$ exhibited a peak temperature of 164 °C with a systematic hydrogen capacity of 3.7 wt.%. More importantly, induced by the synergistic effect of catalysis role of Co NPs and the effective nanoconfinement role of Co-NPC, a reversible systematic capacity of 3.3 wt.% H_2 could still be achieved at a temperature as low as 170 °C after 5 cycles of hydrogenation and dehydrogenation process. This novel strategy could be extended to improve the hydrogen storage performance of various complex hydrides towards practical hydrogen storage application with high energy density.

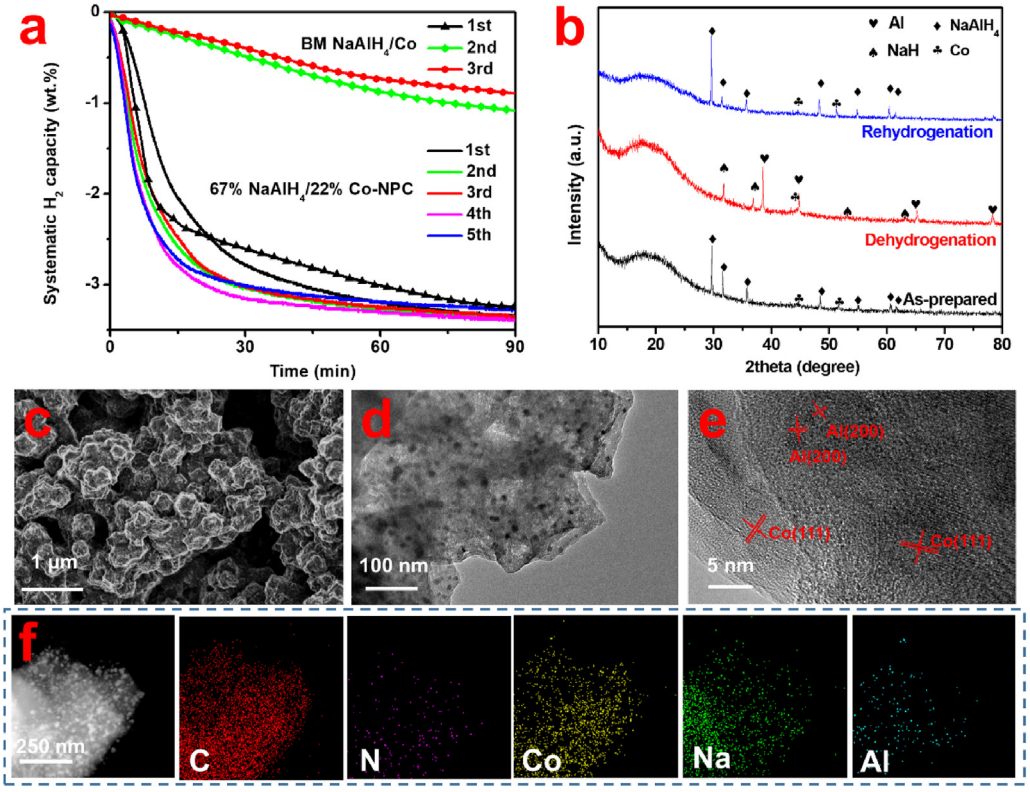

Fig. 6. (a) Cycling hydrogen desorption curves of 67 % $NaAlH_4$/22 % Co-NPC at 170 °C, with ball-milled $NaAlH_4$ catalyzed by Co NPs included for comparison. (b) XRD patterns of the 67 % $NaAlH_4$/22 % Co-NPC after 5 cycles of dehydrogenation and hydrogenation process. (c) SEM, (d) TEM, (e) HRTEM images, and (f) STEM image and the corresponding EDS elemental mapping of 67 % $NaAlH_4$/22 % Co-NPC after 5 cycles of dehydrogenation process.

4. Experimental section

All reagents and solvents were commercially available and used as received without further purification.

4.1. The preparation of Co-NPC

ZIF-67 was prepared as reported in the literature with minor modification [40]. In a typical synthesis, 1.152 g cobalt nitrate and 1.26 g 2-methylimidazole was dissolved separately in 50 ml methanol under magnetic stirring. The solutions were then mixed together under constant stirring for 5 min and were aged at room temperature for 24 h. Subsequently, the precipitate (ZIF-67) was separated by centrifugation and washed with ethanol for 4 times followed by drying under vacuum at 60 °C for overnight. Finally, the Co-NPC was obtained after carbonizing the ZIF-67 crystals under Ar flow at 800 °C for 2 h with a heating rate of 2 °C min^{-1}.

4.2. The preparation of x% Co-NPC

The as-prepared Co-NPC was etched by altering the concentration of HNO_3 and etching time to obtain *x*% Co-NPC. Co-NPC was etched by 3 mol L^{-1} HNO_3 for 3 h, 1 mol L^{-1} for 1 h, and 0.1 mol L^{-1} for 10 min, respectively. All the etched Co-NPCs were then washed with deionized water for 3 times and dried under vacuum at 80 °C for 12 h and reduced in tube finance at 700 °C for 2 h under H_2/Ar atmosphere to remove the possible oxygen-containing groups. All the samples were denoted as *x*% Co-NPC, in which *x* is the mass ratio of Co NPs in the Co-NPC.

4.3. The melt infiltration of $NaAlH_4$

The mixture of $NaAlH_4$ and Co-NPC with various mass ratios was hand-grinded using a mortar and then transferred into a home-made high-pressure autoclave in an Ar-filled glovebox with H_2O and O_2 levels lower than 0.01 ppm. The autoclave was first evacuated and filled with hydrogen to 100 bar at room temperature, which was then heated to 190 °C at a temperature ramp rate of 5 °C min^{-1} and kept for 45 min. After cooling to room temperature, all the melt infiltrated samples were transferred to Ar-filled glovebox, denoted as *y*% $NaAlH_4$/Co-NPC, in which *y* is the mass ratio of $NaAlH_4$ in the composites. The infiltration of $NaAlH_4$ into *x*% Co-NPC was realized according to the similar method and the as-prepared samples were denoted as *y*% $NaAlH_4$/*x*% Co-NPC, in which *x* is the mass ratio of Co NPs in Co-NPC and *y* is the mass ratio of $NaAlH_4$ in the composites.

4.4. The preparation of ball-milled samples

The ball-milled composite of $NaAlH_4$ and Co (denoted as BM $NaAlH_4$/Co) was prepared by ball milling the mixture of $NaAlH_4$ and Co with a weight ratio of 2:1 at 400 rpm for 10 h on a planetary ball mill (QM-3SP4, Nanjing Nanda Instrument Plant). The ball-to-sample ratio was approximately 50:1. The ball-milled $NaAlH_4$ (denoted as BM $NaAlH_4$) was prepared by the same milling process with the absence of Co.

4.5. The preparation of Co nanoparticles

Co NPs were prepared based on a facile reduction method as reported previously [41]. Typically, 0.4 g of $CoCl_2 \cdot 6H_2O$ and 0.2 g of $NaBH_4$ were simultaneously added to 20 ml of deionized water at room temperature. After the complete release of hydrogen, gray–black powders were collected with a magnet, followed by washing with deionized water and ethanol. Co NPs could be obtained after vacuum-drying for 24 h.

4.6. Characterization and testing

A home-built high pressure gas sorption apparatus (HPSA) was used to qualitatively determine the hydrogen desorption performance. Quantitative evaluation of the dehydrogenation/hydrogenation reaction were conducted with the HPSA. For each temperature-dependent dehydrogenation (TPD) test, approximately 30 mg of the as-prepared sample was heated to 260 °C with a temperature ramp rate of 2 °C min^{-1} and an initial pressure lower than 0.001 bar. For isothermal dehydrogenation measurement, the reactor was heated to setting temperature as soon as possible under static vacuum and kept for 90 min. For the cycle performance test, the as-prepared samples were heated to 170 °C rapidly and hold for 90 min under an initial pressure lower than 0.001 bar and the dehydrogenated products were hydrogenated under a hydrogen pressure of 100 bar at 140 °C.

The phase structure of the samples was identified by X-ray diffraction (XRD; D8 advance, Bruker AXS) with Cu K_α radiation at 50 KV and 30 mA. All samples were sealed on sample stage in Ar-filled glovebox with scotch tapes to prevent air and moisture during the test. The morphologies of the samples were observed by scanning electron microscopy (SEM, Shimadzu JEOL 7500FA) and transmission electron microscopy (TEM, JEOL JEM-2100 F). The average particle size of Co NPs in Co-NPC was determined by measuring the particle size of more than 100 particles in relative TEM images using the Nano-Measurer software. Elemental analyses of the materials were also performed by energy-dispersive X-ray spectroscopy (EDS) on TEM. N_2 sorption isotherms were recorded using an ASAP 2020 Plus analyzer (Maxwell Technologies, Inc.) at 77 K. The surface areas were calculated by the Brunauer–Emmett–Teller (BET) method and the pore size distribution was derived from the adsorption branches of the isotherms using the Barrett–Joyner–Halenda (BJH) model.

CRediT authorship contribution statement

Wei Chen: Investigation, Data curation, Formal analysis, Writing - original draft. **Lei You:** Investigation, Methodology. **Guanglin Xia:** Conceptualization, Methodology, Supervision, Writing - review & editing. **Xuebin Yu:** Supervision, Writing - review & editing.

Declaration of Competing Interest

The authors report no declarations of interest.

Acknowledgements

This work was partially supported by the National Key R&D Program of China (No. 2018YFB1502101), National Science Fund for Distinguished Young Scholars (51625102), the National Natural Science Foundation of China (51971065, 51901045), the Innovation Program of Shanghai Municipal Education Commission (2019-01-07-00-07-E00028), the Open Fund of the Guangdong Provincial Key Laboratory of Advanced Energy Storage Materials, and the Programs for Professor of Special Appointment (Eastern Scholar) at Shanghai Institutions of Higher Learning.

Appendix A. Supplementary data

Supplementary material related to this article can be found, in the online version, at doi:https://doi.org/10.1016/j.jmst.2020.11.052.

References

[1] L.Z. Ouyang, W. Chen, J.W. Liu, M. Felderhoff, H. Wang, M. Zhu, Adv. Energy Mater. 7 (2017) 1700299.
[2] Y.Y. Zhu, L.Z. Ouyang, H. Zhong, J.W. Liu, H. Wang, H.Y. Shao, Z.G. Huang, M. Zhu, Angew. Chem. Int. Ed. 59 (2020) 8623–8629.
[3] G.L. Xia, Y.B. Tan, X.W. Chen, D.L. Sun, Z.P. Guo, H.K. Liu, L.Z. Ouyang, M. Zhu, Adv. Mater. 27 (2015) 5981–5988.
[4] K. Chen, L.Z. Ouyang, H. Zhong, J.W. Liu, H. Wang, H.Y. Shao, Y. Zhang, M. Zhu, Green Chem. 21 (2019) 4380–4387.
[5] A. Schneemann, J.L. White, S.Y. Kang, S. Jeong, L.F. Wan, E.S. Cho, T.W. Heo, D. Prendergast, J.J. Urban, B.C. Wood, Chem. Rev. 118 (2018) 10775–10839.
[6] X.B. Yu, Z.W. Tang, D.L. Sun, L.Z. Ouyang, M. Zhu, Prog. Mater. Sci. 88 (2017) 1–48.
[7] S. Orimo, Y. Nakamori, J.R. Eliseo, A. Züttel, C.M. Jensen, Chem. Rev. 107 (2007) 4111–4132.
[8] T. He, H.J. Cao, P. Chen, Adv. Mater. 31 (2019) 1902757.
[9] K.T. Møller, D. Sheppard, D.B. Ravnsbæk, C.E. Burckley, E. Akiba, H.W. Li, T.R. Jensen, Energies 10 (2017) 1645.
[10] H.Y. Zhang, G.L. Xia, J. Zhang, D.L. Sun, Z.P. Guo, X.B. Yu, Adv. Energy Mater. 8 (2018) 1702975.
[11] Y.Q. Huang, G.L. Xia, J. Zhang, Z.P. Guo, X.B. Yu, Energy Storage Mater. 17 (2019) 178–185.
[12] Y.F. Liu, Z.H. Ren, X. Zhang, N. Jian, Y.X. Yang, M.X. Gao, H.G. Pan, Energy Technol. 6 (2018) 487–500.
[13] J.O. Jensen, Q.F. Li, R.H. He, C. Pan, N. Bjerrum, J. Alloys Compd. 404 (2005) 653–656.
[14] R.Y. Wu, H.F. Du, Z.Y. Wang, M.X. Gao, H.G. Pan, Y.F. Liu, J. Power Sources 327 (2016) 519–525.
[15] Y.F. Liu, X. Zhang, K. Wan, Y.X. Yang, M.X. Gao, H.G. Pan, J. Mater. Chem. A 4 (2016) 1087–1095.
[16] X. Zhang, Y.F. Liu, K. Wang, M.X. Gao, H.G. Pan, Nano Res. 8 (2015) 533–545.
[17] X. Zhang, Y.F. Liu, Y.P. Pang, M.X. Gao, H.G. Pan, J. Mater. Chem. A 2 (2014) 1847–1854.
[18] X. Zhang, Z.H. Ren, Y.H. Lu, J.H. Yao, M.X. Gao, Y.F. Liu, H.G. Pan, ACS Appl. Mater. Interfaces 10 (2018) 15767–15777.
[19] Y.P. Wang, Q.L. Ren, Y.J. Wang, L. Li, D.W. Song, L.F. Jiao, H.T. Yuan, Int. J. Hydrogen Energy 35 (2010) 11004–11008.
[20] C.K. Huang, Y.J. Zhao, T. Sun, J. Guo, L.X. Sun, M. Zhu, J. Phys. Chem. C 113 (2009) 9936–9943.
[21] M.P. Pitt, P.E. Vullum, M.H. Sørby, H. Emerich, M. Paskevicius, C.E. Burkley, J.C. Walmsley, R. Holmestad, B.C. Hauback, J. Phys. Chem. C 116 (2012) 14205–14217.
[22] J.J. Liu, Y. Han, Q.F. Ge, Chem.–Eur. J. 15 (2009) 1685–1695.
[23] S.S.Y. Lin, J. Yang, H.H. Kung, Int. J. Hydrogen Energy 37 (2012) 2737–2741.
[24] X. Zhang, Z.H. Ren, X.L. Zhang, M.X. Gao, H.G. Pan, Y.F. Liu, J. Mater. Chem. A 7 (2019) 4651–4659.
[25] Y.F. Liu, C. Liang, H. Zhou, M.X. Gao, H.G. Pan, Q.D. Wang, Chem. Commun. 47 (2011) 1740–1742.
[26] X. Zhang, X.L. Zhang, Z.H. Ren, J.J. Hu, M.X. Gao, H.G. Pan, Y.F. Liu, Front. Chem. 8 (2020) 419.
[27] P. Adelhelm, J.B. Gao, M.H. Verkuijlen, C. Rongeat, M. Herrich, P.J.M. van Bentum, O. Gutfleisch, A.P. Kentgens, K.P. de Jong, P.E. de Jongh, Chem. Mater. 22 (2010) 2233–2238.
[28] R. Palm, H. Kurig, J. Aruväli, E. Lust, Microporous Mesoporous Mater. 264 (2018) 8–12.
[29] Y.T. Li, G. Zhou, F. Fang, X.B. Yu, Q. Zhang, L.Z. Ouyang, M. Zhu, D.L. Sun, Acta Mater. 59 (2011) 1829–1838.
[30] C.L. Carr, W. Jayawardana, H.Y. Zou, J.L. White, F.E.I. Gabaly, M.S. Conradi, V. Stavila, M.D. Allendorf, E.H. Majzoub, Chem. Mater. 30 (2018) 2930–2938.
[31] Q.L. Gao, G.L. Xia, X.B. Yu, Nanoscale 9 (2017) 14612–14619.
[32] X.L. Fan, X.Z. Xiao, J. Shao, L.T. Zhang, S.Q. Li, H.W. Ge, Q.D. Wang, L.X. Chen, Nano Energy 2 (2013) 995–1003.
[33] P. Javadian, T.K. Nielse, D.B. Ravnsbaek, L.H. Jepsen, M. Polanski, T. Plocinski, L. Kunce, F. Besenbacher, J. Bystrzycki, T.R. Jensen, J. Solid State Chem. 231 (2015) 190–197.
[34] T.K. Nielsen, M. Polanski, D. Zasada, P. Javadian, F. Besenbacher, J. Bystrzycki, J. Skibsted, T. Jensen, ACS Nano 5 (2011) 4056–4064.
[35] V. Stavila, R.K. Bhakta, T.M. Alam, E.H. Majzoub, M.D. Allendorf, ACS Nano 6 (2012) 9807–9817.
[36] M. Paskevicius, U. Filsø, F. Karimi, J. Puszkiel, P.K. Prazas, C. Pistidda, A. Hoell, E. Welter, A. Schreyer, T. Klassen, Int. J. Hydrogen Energy 41 (2016) 4159–4167.
[37] R.J. Xiong, G. Sang, X.Y. Yan, G.H. Zhang, X.Q. Ye, J. Mater. Chem. 22 (2012) 17183–17189.
[38] X.D. Kang, Z.Z. Fang, L.Y. Kong, H.M. Cheng, X.D. Yao, G.Q. Yao, P. Wang, Adv. Mater. 20 (2008) 2756–2759.
[39] Y.T. Li, F. Fang, H.L. Fu, J.M. Qiu, Y.S. Li, D.L. Sun, Q.A. Zhang, L.Z. Ouyang, M. Zhu, J. Mater. Chem. A 1 (2013) 5238–5246.
[40] J.F. Qian, F.A. Sun, L.Z. Qin, Mater. Lett. 82 (2012) 220–223.
[41] X.M. Liang, L.J. Zhao, RSC Adv. 2 (2012) 5485–5487.